ACS NANO
Cite This: ACS Nano 2017, 11, 10785-10796
www.acsnano.org

ARTICLE

Low-Temperature Single Carbon Nanotube Spectroscopy of sp^3 Quantum Defects

Xiaowei He,[†] Brendan J. Gifford,[‡,∥] Nicolai F. Hartmann,[†] Rachelle Ihly,[§] Xuedan Ma,[†] Svetlana V. Kilina,[∥] Yue Luo,[⊥] Kamran Shayan,[⊥] Stefan Strauf,[⊥] Jeffrey L. Blackburn,[§] Sergei Tretiak,[†,‡] Stephen K. Doorn,*[,†] and Han Htoon*[,†]

[†]Center for Integrated Nanotechnologies, Materials Physics and Applications Division, and [‡]Theoretical Division and Center for Nonlinear Studies, Los Alamos National Laboratory, Los Alamos, New Mexico 87545, United States

[§]Chemical and Materials Science Center, National Renewable Energy Laboratory, 1617 Cole Boulevard, Golden, Colorado 80401, United States

[∥]Department of Chemistry and Biochemistry, North Dakota State University, Fargo, North Dakota 58108, United States

[⊥]Department of Physics, Stevens Institute of Technology, Hoboken, New Jersey 07030, United States

Supporting Information

ABSTRACT: **Aiming to unravel the relationship between chemical configuration and electronic structure of sp^3 defects of aryl-functionalized (6,5) single-walled carbon nanotubes (SWCNTs), we perform low-temperature single nanotube photoluminescence (PL) spectroscopy studies and correlate our observations with quantum chemistry simulations. We observe sharp emission peaks from individual defect sites that are spread over an extremely broad, 1000−1350 nm, spectral range. Our simulations allow us to attribute this spectral diversity to the occurrence of six chemically and energetically distinct defect states resulting from topological variation in the chemical binding configuration of the monovalent aryl groups. Both PL emission efficiency and spectral line width of the defect states are strongly influenced by the local dielectric environment. Wrapping the SWCNT with a polyfluorene polymer provides the best isolation from the environment and yields the brightest emission with near-resolution limited spectral line width of 270 μeV, as well as spectrally resolved emission wings associated with localized acoustic phonons. Pump-dependent studies further revealed that the defect states are capable of emitting single, sharp, isolated PL peaks over 3 orders of magnitude increase in pump power, a key characteristic of two-level systems and an important prerequisite for single-photon emission with high purity. These findings point to the tremendous potential of sp^3 defects in development of room temperature quantum light sources capable of operating at telecommunication wavelengths as the emission of the defect states can readily be extended to this range *via* use of larger diameter SWCNTs.**

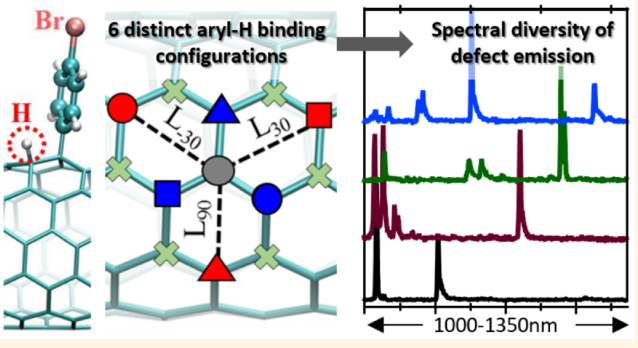

KEYWORDS: *carbon nanotubes, electronic structure, diazonium doping, photoluminescence, exciton localization*

Materials scientists and chemists intentionally incorporate impurities and defects as a powerful tool for modification of electronic and optical properties of host materials.[1] In semiconductor nanostructures, this approach can be used to introduce optically active quantum states that enable a wide range of novel functionalities. For example, doping of quantum dots and quantum wells with Mn^{2+} enables spin-electronics and spin-photonics.[2] Rare-earth-doped nanocrystals also facilitate new developments in displays, solid-state lasers, catalysis, and biological labeling.[3] Nitrogen and silicon vacancy centers introduced into diamond and SiC hosts have also brought transformational advances in applications ranging from ultrasensitive sensing of electric/magnetic fields to realization of quantum computing and communication technologies.[4−6] Recent studies have shown that such introduction of quantum states is also possible in semiconducting single-walled carbon nanotubes (SWCNTs) through low-level covalent attachment of various chemical functional groups such as ether/epoxide[7−10] and a variety of monovalent and divalent alkyl and aryl functionalities with varying complexities introduced through versatile diazonium

Received: May 2, 2017
Accepted: September 28, 2017
Published: September 28, 2017

DOI: 10.1021/acsnano.7b03022
ACS Nano 2017, 11, 10785−10796

and halide reactive groups.[11−14] While the molecular structures of functional groups vary widely, all of these lead to creation of sp^3 defects that strongly localize the band-edge excitons into quantum states located 100−300 meV below the first bright band-edge exciton level (E_{11}).[7−15] While most defects of SWCNTs are typically known for quenching photoluminescence, these quantum states of the sp^3 defects, which we will refer to as quantum defects or defect states, can enhance SWCNT emission efficiency by more than an order of magnitude (from <1% up to 28%).[8,11] Such dramatic enhancement makes envisioned applications of SWCNTs in optoelectronics, sensing, and imaging technologies more feasible. Furthermore, due to their introduction of a very deep confinement potential, these defect states are also expected to maintain their quantum mechanical characteristics, such as single-photon emission, up to room temperature. In line with this expectation, room temperature single-photon emission[16] and tunability of this quantum light emission to 1.55 μm,[17] were recently demonstrated. This unique property of quantum defects in SWCNTs, together with their compatibility with Si-based nanodevice fabrication technology,[10,18,19] opens a new path to realize room temperature single-photon sources operating at telecommunication wavelengths that are critically needed for applications in quantum communications.

Realization of this tremendous potential demands a detailed understanding of the electronic structure and chemical nature of these defect states. So far, such understanding has been attained only for a small subset of quantum defects, namely, those introduced by attachment of ether and epoxide functional groups.[7,8,20] Among the growing number of defect varieties, attachment of aryl groups (*e.g.*, benzene, 4-bromobenzene, 4-methoxybenzene, 3,5-dichlorobenzene, *etc.*) *via* diazonium chemistry has attracted significant attention from chemists.[11,21] An advantage of such functionalization is that the reaction chemistry is easy to implement and control, while providing significant room for synthetic modification of the defect-state properties to tune emission energies and directly pair the exciton localization properties of the defect site with multifunctional behaviors such as associated sensing capability.[15] Beyond the monovalent aryl diazonium agents, several additional classes of monovalent and divalent alkyl and aryl iodide and more complex aryl defects have been introduced.[12−14] This variability has in turn led to a diversity in optical behavior of defect states. The series of aryl and alkyl iodide agents introduced by Kwon *et al.*[14] generates defect-state spectra dominated by a single emission band spanning between 1100 and 1170 nm for (6,5) SWCNTs. In contrast, both complex divalent diazonium species[13] and alkyl bromide agents[12] are found to introduce two emission bands—the first between 1100 and 1170 nm and a second emission band with a larger red shift at 1220−1290 nm. Different structures modulate the relative intensities of the two observed defect bands, for which the lower energy state can dominate the spectrum in some cases.[12,13] Spectra for monovalent aryl defects initially appear as simple single-peak features, but closer inspection reveals the appearance of deeper states, although with relatively weak intensity.[11,22] The origins of these multipeaked spectra are yet to be rationalized by establishing important links relating electronic properties of the functional groups to their respective surface chemistries. Here, the monovalent aryl defects serve as a useful model system for such studies.

This rich chemical diversity and complex electronic structure presents an exciting opportunity, not only to manipulate the energy of the defect states but also to define the complexity of their excitonic and spin fine structure to accommodate spintronic[2] and quantum technology applications.[23,24] Harnessing this potential requires a detailed understanding of the relationship between chemical binding configuration and electronic structure of functionalized SWCNTs. The fundamental characteristics of optical transitions such as intrinsic shape and widths of spectral lines also must be determined in correlation with electronic structure and chemical configuration. Because of inhomogeneous and thermal broadening effects, these intrinsic characteristics of defect states cannot be attained in conventional optical spectroscopy studies performed on solution-suspended functionalized SWCNT ensembles.

To this end, we have performed low-temperature photoluminescence spectroscopies on individual aryl defect states created on (6,5) SWCNTs through diazonium functionalization chemistry and correlate the results with excited-state electronic structure simulations. The experiment reveals sharp PL peaks that are inhomogeneously distributed over a very wide, 1000−1350 nm, spectral range. Simulations for (6,5) SWCNTs functionalized with monovalent aryl groups identify 6 topologically distinct binding configurations, each having unique electronic structure and emission wavelength. Based on a qualitative correlation between the spectral ranges of the experimentally observed PL peaks and the energy distribution of calculated emissive states, we attribute the existence of 6 distinct binding configurations as the source of the observed inhomogeneous distribution. We also have observed that well-isolated quantum defect states created in PFO-BPy-wrapped SWCNTs can emit near resolution-limited emission lines with a full-width at half-maximum (fwhm) as narrow as 270 μeV, with well-resolved acoustic phonon wings. The narrow line width and the emission energy distribution of defect states are found to be highly dependent on the dielectric environment. These findings, together with those reported for quantum states of oxygen-functionalized SWCNTs in prior studies,[7,10,16,25] lay a foundation toward building a generalized understanding of the emergence of novel optical behavior from quantum defect states, which can be created *via* multiple chemical functionalization routes.[12−14] Such understanding could lead to a rational strategy toward controllable creation and manipulation of individual covalent quantum defects with desired optical functionalities.

RESULTS AND DISCUSSION

In order to attain a comprehensive understanding of optical characteristics and their dependence on environment, we performed our single tube spectroscopic studies on aryl defect states in different environments. Specifically, defect states were introduced on sodium deoxycholate (DOC) and polyfluorene polymer (PFO-BPy)-wrapped (6,5) SWCNTs. A conventional aqueous solution-phase diazonium-based functionalization process was utilized to introduce two different types of aryl functional groups (4-methoxybenzene and 3,5-dichlorobenzene) onto DOC-wrapped SWCNTs.[11,22,26] For PFO-BPy-wrapped SWCNTs, which are not amenable to the solution-phase process nor to functionalization with the 4-methoxybenzene diazonium reagents, we developed a dip-doping approach to introduce 3,5-dichlorobenzene aryl groups, as described in detail in the Methods section. The functionalized SWCNTs are spread on varying substrates, including glass

DOI: 10.1021/acsnano.7b03022
ACS Nano 2017, 11, 10785−10796

coverslips, coverslips spin-coated with a 160 nm polystyrene layer, and sandwiched between two polystyrene layers placed on top of a coverslip with a density of ~1 nanotube/4 μm^2.

Low-Temperature Photoluminescence (PL) Spectroscopy of Individual PFO-BPy-Wrapped 3,5-Dichlorobenzene-Functionalized SWCNTs on Glass. Figure 1a shows nine single SWCNT PL spectra out of more than 60 investigated. The average of all 60 spectra is displayed in comparison with an ensemble PL spectrum taken from a film of functionalized SWCNTs at room temperature (RT) in Figure 1b (black and green, respectively). The RT ensemble spectrum shows E_{11} exciton emission around ~1000 nm and the main defect-state emission peak at 1160 nm with a tail extending toward 1300 nm. While individual unfunctionalized SWCNTs display a single sharp isolated E_{11} exciton emission peak (see Figure S2 of Supporting Information of ref 7), low-T PL spectra for individual functionalized SWCNTs (Figure 1a) show multiple sharp peaks that are distributed throughout the 1000−1350 nm spectral range. Each of the peaks is found to be in a similar range of PL intensity, irrespective of their emission wavelength. As a result, an accumulated average of these single tube spectra reflects the distribution of the PL peak density that we observe. Furthermore, this peak distribution appears very broad and nearly featureless, as shown in Figure 1b (black line). This broad inhomogeneous distribution stands in contrast with that reported for oxygen-functionalized SWCNTs, for which three inhomogeneous peak distributions could readily be resolved.[7] In the oxygen case, each distribution could be directly associated with quantum states of three distinct oxygen functional groups. This contrast in spectral behavior provides some indications that attachment of aryl groups may create a larger number of energetically distinct quantum states than in the case of oxygen functionalization.

Quantum Chemistry Simulations. In order to attain further insight into this spectral diversity, we performed electronic structure calculations using density functional theory (DFT) and time-dependent DFT (TD-DFT) (see Methods). In brief, DFT simulations provide us with energies and geometric structures at the ground state, whereas TD-DFT modeling evaluates the same quantities for electronically excited states and evaluates spectroscopic properties. Covalent attachment of an aryl group (here only 4-bromobenzene is considered for simplicity) leads to an intermediate in which the bound aryl group is accompanied by a reactive electron located on a nearby SWCNT carbon atom. In our aqueous environment, this excess site likely captures a proton resulting in overall divalent binding, where two carbons on the SWCNT surface formally adapt sp^3 conformation and the entire tube preserves a neutral closed shell configuration. This leads to the possibility of several binding sites of both aryl and hydrogen (aryl-H) attached to the same carbon ring on the (6,5) sidewall. The bound proton can be located either adjacent to the site of the initial aryl addition ("ortho") or three carbon atoms away ("para") (see Figure 2a), leading to six chemically distinct aryl-H configurations. The configurations marked as "meta" (*i.e.*, two carbons away) are not plausible due to the lack of a reactive intermediate with a deficit of charge density on the "meta" position with respect to the aryl binding site, as well established in aromatic reaction chemistry. They are therefore precluded from consideration. Our previous simulations[20,21] show that any alternative binding configurations other than discussed above, result in multiple optically inactive low-energy transitions across the gap, precluding appearance of emissive species. A similar situation holds for all monovalent intermediates with unpaired reactive electron(s) lacking binding to a proton. Therefore, only 6 aryl-H configurations with both functionalized sp^3 carbons located at the same six-membered ring of the SWCNT are considered in this study.

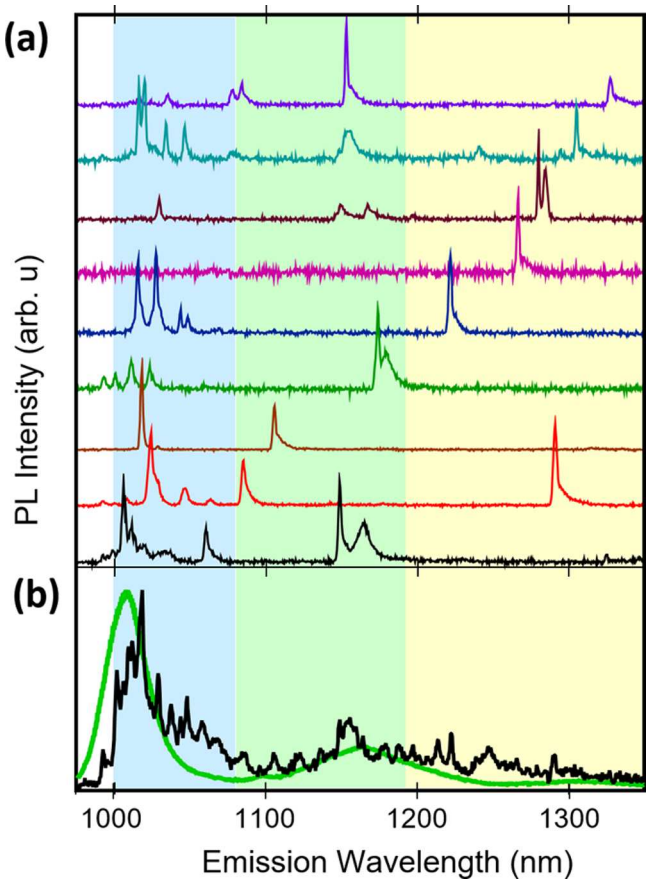

Figure 1. (a) Low-temperature PL spectra of 9 individual 3,5-dichlorobenzene-functionalized (6,5) SWCNTs wrapped in PFO-BPy. (b) Black and green lines: average low-T PL spectrum of 60 individual 3,5-dichlorobenzene-functionalized SWCNTs and ensemble, RT PL spectrum of functionalized SWCNT film, respectively. Based on DFT simulations (see Figure 2), we tentatively attribute PL peaks in the three colored bands to different aryl binding configurations. Peaks in the blue band may be attributed to transitions for the ParaL_{30} and OrthoL_{-30} binding configurations (some peaks in the 1000−1030 nm range may also originate from the E_{11} transition), those in the green band to the OrthoL_{90}, and those in the yellow band to the ParaL_{90}, OrthoL_{30}, and ParaL_{-30} transitions, respectively.

Our quantum chemical calculations reveal that these 6 aryl-H configurations are different chemical species in terms of the interaction strength between the functional group and the tube surface, as well as in terms of electronic structures and optically allowed transitions, which ultimately define the observed emission properties. Specifically, as shown in Figure 2a, we have calculated three distinct Para and Ortho configurations, which are identified according to the direction of aryl-H arrangement relative to the SWCNT lattice and labeled as L_{30}, L_{90}, and L_{-30}. It is important to note that the chemical uniqueness of each configuration is, in part, defined by the SWCNT chiral structure. The relative energy difference between configurations is less than 0.4 eV, with the most stable being the L_{-30} and L_{30} in Ortho configurations, while the

DOI: 10.1021/acsnano.7b03022
ACS Nano 2017, 11, 10785−10796

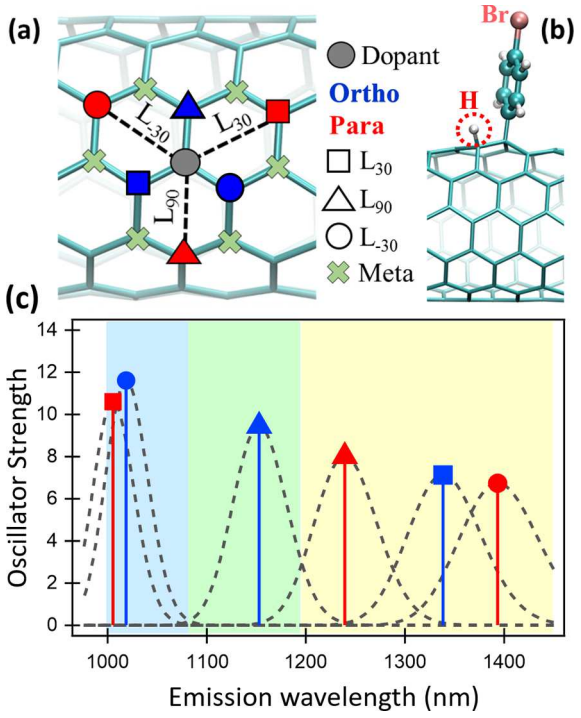

Figure 2. (a) Top view of a (6,5) SWCNT, showing an aryl defect site (gray circle) and locations of allowed (circle, triangle, square) and forbidden (cross) sites for capture of hydrogen. Hydrogen capture sites immediately next to the dopants (blue) are marked Ortho and those at 3-carbon atoms away (red) are marked Para. Three Ortho and Para sites are further classified according to their bonding orientations marked as L_{30} (square), L_{90} (triangle), and L_{-30} (circle). (b) Side view of a (6,5) nanotube, a bound 4-bromobenzene group, and a hydrogen atom. (c) Plot showing oscillator strength and emission wavelength of the lowest emissive state of ParaL_{30}, OrthoL_{-30}, OrthoL_{90}, ParaL_{90}, OrthoL_{30}, and ParaL_{-30} transitions for (6,5) functionalized with 4-bromobenzene. Ortho and Para transitions are plotted in blue and red, respectively. The three different bond angles of 30, −30, and 90° are marked in the same way as in (a). Dashed Gaussian curves show the inhomogeneous distribution expected for each transition. Based on these inhomogeneous distributions, blue band (1000−1080 nm) is tentatively assigned for the ParaL_{30} and OrthoL_{-30} transitions, the green band (1080−1190 nm) for the OrthoL_{90}, and the yellow band (>1190 nm) for ParaL_{90}, OrthoL_{30}, and ParaL_{-30} transitions, respectively.

least stable structure is ParaL_{-30} (see Figure S1, Supporting Information). As it is known that aryl diazonium salts have very complex chemistry in solutions due to the variety of reaction pathways with a large number of potential intermediate products,[27−29] we assume that all six configurations can take place and coexist in experimental samples.

The 4-bromobenzene considered for our calculation differs in chemical group attached to the benzene ring from the 4-methoxybenzene and 3,5-dichlorobenzene used in our experiments. Slight differences in electronegativity associated with each of the substituents is expected to introduce only minor differences in the electronic structure of each specific defect type,[11] due to the nonpolar character of the SWCNT. In fact, recent PL studies on solutions of 4-methoxybenzene and 3,5-dichlorobenzene-functionalized (6,5) SWCNTs show defect-state emission peaks that are shifted from one another by only 10 meV.[22] Furthermore, our additional simulations for variations of the chemical structure of the functional group (presented in the Supporting Information: pristine aryl *vs* 4-bromobenzene in Figure S2 and hydrogen *vs* hydroxide in Figure S3) demonstrate minimal uniform shifts of the HOMO−LUMO gap and optical spectra by not more than 10 meV for all considered defect conformations (see technical details in Methods). Therefore, 4-bromobenzene is a representative model for comparison to the experimental systems.

Using TD-DFT, we simulate absorption spectra and optimize the lowest-energy state to evaluate emission energy, oscillator strengths, and redistribution of the transition density reflecting the spatial extent of the respective excitonic states. It is well-known that the absolute values of these observables are sensitive to the density functional and the basis set, while the qualitative trends are typically method independent.[30] We have used the long-range corrected functional CAM-B3LYP that reasonably reproduces the essential excitonic physics in carbon-based low-dimensional materials, while it tends to overestimate the absolute transition energies.[31,32] Furthermore, confinement effects, due to the necessity of modeling a finite length of SWCNT (~12 nm), also introduce an additional blue-shift of the calculated transitions, compared to those of the μm long counterparts used in our experimental samples. Thus, to directly compare experimental and calculated optical spectra, we have scaled the calculated absorbing as well as emissive transition energies (*e.g.*, Figure S4, Supporting Information) using our experimental value for the E_{11} transition energy as the reference point, as described in detail in the Methods and Supporting Information.

Experiment−Theory Correlations. The most important results from modeling of the aryl-H emissive states are shown in Figure 2c. Our calculations predict the lowest energy emissive states at 1005, 1019, 1153, 1239, 1338, and 1393 nm for ParaL_{30}, OrthoL_{-30}, OrthoL_{90}, ParaL_{90}, OrthoL_{30}, and ParaL_{-30}, respectively. Their oscillator strengths slightly decrease as their energy red shifts from the E_{11} band-edge exciton (this energy difference is dubbed the trapping energy). The delocalization of the transition density, reflecting the exciton wave function spread over the nanotube, follows the same trend of decreasing with increasing trapping energies, as illustrated in Figure S5, Supporting Information. This increasing exciton localization with an increased trapping energy explains the slight, concomitant reduction of the oscillator strength. Incorporation of environmental effects into our calculations at the level of the Polarizable Continuum model (PCM)[33] leads to 10−30 meV shifts for the optical transitions (Figure S6, Supporting Information). While this shift is uniform and systematic for the SWCNTs in different solvents, it gives rise to an inhomogeneous distribution in our single tube experiment because the dielectric environment of individual tubes is known to vary widely from one to another due to substrate interactions. Our prior study showed that this effect can introduce inhomogeneous broadening up to 60 meV in fwhm of oxygen defect peak distributions.[7] Assuming that the inhomogeneous distribution is similar in the case of aryl functionalization, we overlaid such a Gaussian broadening on the distribution of emission peaks expected to be observed for our calculated transitions in Figure 2c as the dashed lines.

The theoretically simulated emissive states spread over a wide wavelength range, from 1000 to 1400 nm. This spread is in qualitative agreement with the spectral diversity of PL peaks observed in Figure 1 (1000−1350 nm). This qualitative agreement leads us to conclude that the observed spectral

DOI: 10.1021/acsnano.7b03022
ACS Nano 2017, 11, 10785−10796

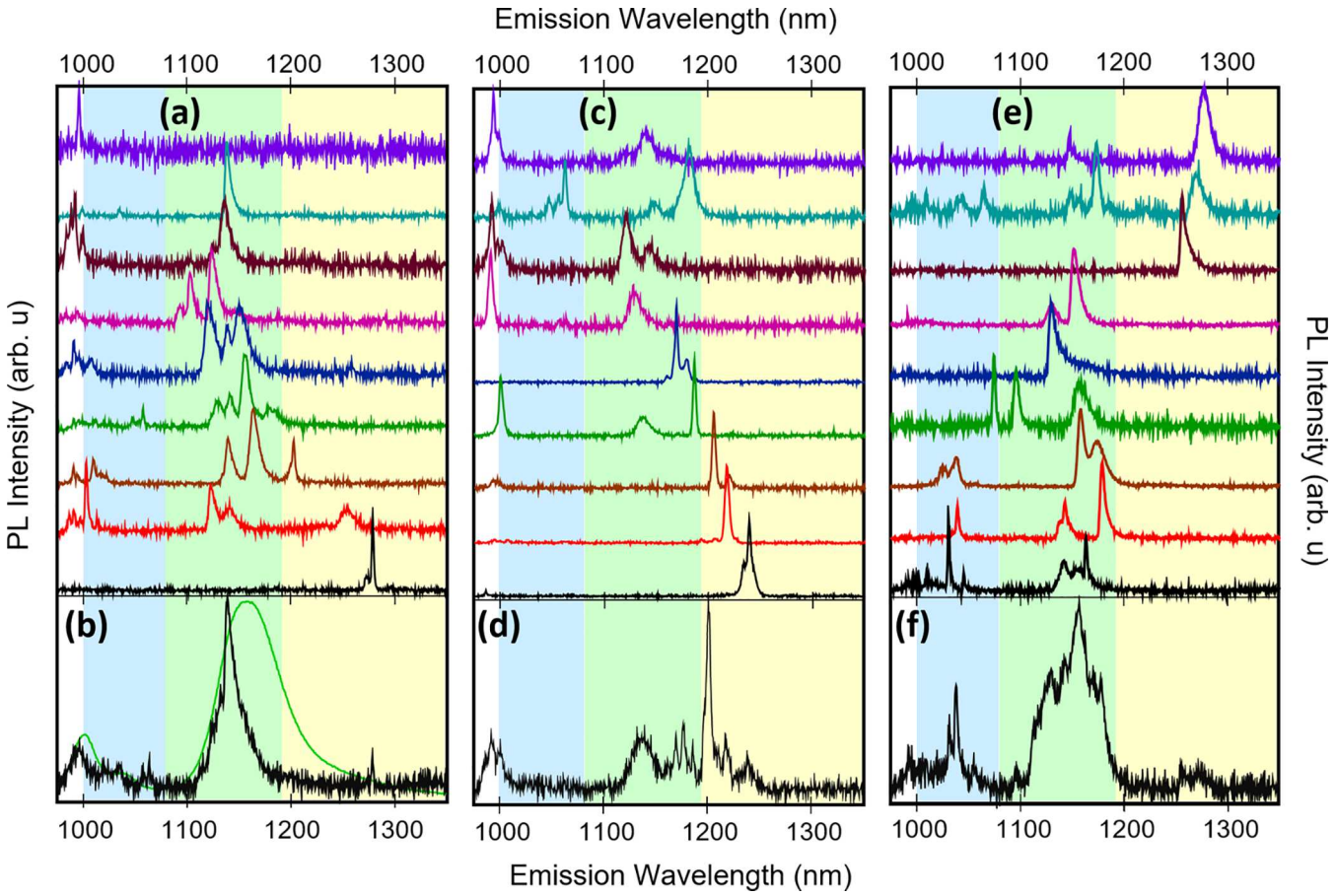

Figure 3. Low-temperature PL spectra of 9 individual DOC-wrapped 4-methoxybenzene-functionalized SWCNTs deposited directly on glass (a), on 160 nm thick polystyrene layer (c), and sandwiched between two polystyrene layers (e), and average spectra (b,d,f) calculated from 40, 39, and 40 functionalized SWCNTs of (a,c,e), respectively. Room temperature, solution-phase PL spectrum of functionalized SWCNT in 1% aqueous DOC is plotted in (b) as a green line. Blue, green, and yellow spectral bands of Figure 2 are overlaid on the spectra. The data for the 4-methoxybenzene aryl group instead of the dichlorobenzene aryl group were chosen to show that the observed environmental effect and broad spectral diversity is a general result for the entire class of aryl sp^3 defects. A control experiment with dichlorobenzene-functionalized SWCNTs (displayed as Figure S8) shows similar results.

diversity is a direct consequence of the existence of the expected six distinct chemical configurations. Furthermore, while the noted limitations of the calculation and the existence of an inhomogeneous distribution for each emissive state prevent us from unambiguously assigning an observed PL peak to a specific transition, we can tentatively attribute defect peaks appearing in the 1000−1080 nm range (blue band in Figure 1) to the $ParaL_{30}$ and $OrthoL_{-30}$ transitions, those in the 1080 to 1190 nm range (green band) to the $OrthoL_{90}$ transition and those beyond the 1190 nm range (yellow band) to the $ParaL_{90}$, $OrthoL_{30}$, and $ParaL_{-30}$ transitions, respectively. For features appearing within the blue band, it is important to note that the E_{11} band-edge exciton emission (~980−1030 nm) also likely overlaps this region, thus complicating assignment of features at the short-wavelength edge of this range. The shape of the average PL spectrum indicates that while all six configurations are likely to occur and contribute to PL emission, defects with deeper trapping energies (*i.e.*, $ParaL_{90}$, $OrthoL_{30}$ and $ParaL_{-30}$) occur at lower probability compared to the others. The observation that a single tube can display multiple sharp peaks that fall in the spectral bands of the transitions predicted for different aryl-H configurations (*e.g.*, top 3 spectra of Figure 1a) indicates that multiple aryl-H sites, each with a different binding configuration, can coexist on a given nanotube within the <1 μm spatial resolution of our experiment. Because only 5−6 peaks maximum are observed per nanotube, individual defects could still be separated by hundreds of nm, which presumes vanishing interdefect interactions to influence spectra.

Influence of Dielectric Environments. In order to investigate the influence of the dielectric environment upon optical characteristics of the quantum defects, we extended our studies to DOC-wrapped SWCNTs, which are functionalized with 4-methoxybenzene and placed in three different environments: spread directly on a glass substrate (Figure 3a,b), on a 160 nm thick polystyrene film (Figure 3c,d), and completely encapsulated in polystyrene (Figure 3e,f), respectively. For comparison, a typical solution-phase, RT, PL spectrum of doped SWCNTs in 1% aqueous DOC is shown in Figure 3b (green line). The solution spectrum shows a strongly suppressed E_{11} emission peak at ~1000 nm and the main defect emission peak at ~1160 nm with a tail extending to 1300 nm. Importantly, our data reveal that each dielectric environment leads to a unique spectral composition, with the emission of peaks in particular spectral ranges being more pronounced in certain environments. While a large number of PL peaks appear in the 1080−1190 nm green spectral band, tentatively matching the $OrthoL_{90}$ aryl-H configuration in all three environments (Figure 3), the population of PL peaks in other spectral bands

DOI: 10.1021/acsnano.7b03022
ACS Nano 2017, 11, 10785−10796

varies with the environment. Specifically, when the SWCNTs were spread directly on glass, only one of 50 PL peaks observed from 40 individual SWCNTs showed emission in the yellow band beyond 1190 nm that could be attributed to the $ParaL_{90}$, $OrthoL_{30}$, and $ParaL_{-30}$ aryl-H configurations (Figure S7b). PL peaks of all the SWCNTs also exhibit significantly lower intensity compared to those observed in the other two experiments. As a result, the average spectrum shows a single peak in the green band (Figure 3b). For SWCNTs spread on a 160 nm thick polystyrene film, ~15 out of 46 PL peaks observed from 39 SWCNTs displayed strong and sharp emission peaks in the yellow band of the $ParaL_{90}$, $OrthoL_{30}$, and $ParaL_{-30}$ aryl-H configurations (3 bottom spectra of Figure 3c and Figure S7c). For 40 SWCNTs fully encapsulated in polystyrene, while the largest number of PL peaks were still observed in the green band, coinciding with the $OrthoL_{90}$ aryl-H band, PL peaks in the 1000−1080 nm blue band, attributable to the $OrthoL_{-30}$ and $ParaL_{30}$ aryl-H configurations (first−third and eighth spectra from top of Figure 3e and Figure S7d), as well as those in the yellow band of the $ParaL_{90}$, $OrthoL_{30}$, and $ParaL_{-30}$ transitions, become observable. Measurements performed on 3,5-dichlorobenzene-functionalized SWCNTs sandwiched between two polystyrene layers also yield results (Figure S8) very similar to those displayed in Figure 3e,f. These findings are consistent with prior room temperature PL studies of aryl-functionalized SWCNT solutions showing that changing of the specific aryl functional group has only a minor impact on the optical characteristics of the defect states.[11,22] They, furthermore, show that broad spectral diversity originated from 6 binding configurations (and associated emitting states) is a general result for the sp^3 aryl defects.

Because the 1080−1190 nm band of the $OrthoL_{90}$ transition appears predominantly in all three environments, as well as in RT solution spectra (Figure 3b, green line), we can conclude that the solution doping approach preferentially creates the $OrthoL_{90}$ aryl-H configuration. This specifically suggests that the surface structures generated by surfactants (*e.g.*, SDS and DOC) create some degree of selectivity or preference for specific binding configurations. The significant difference in appearance of PL peaks in other emission bands, on the other hand, indicates that the dielectric environment affects the relative emission intensities arising from each type of aryl-H quantum defect in each experiment of Figure 3. Such a result could arise if the functionalized nanotube samples contain different ratios of aryl-H configurations. We can, however, rule out this possibility since all samples studied in Figure 3 were generated from the same solution of functionalized SWCNTs. As the three experiments differ only in the environment in which the samples are deposited, we conclude that these differing environments are the primary factors modifying spectral weighting of different aryl-H configurations. While it is unlikely that the sample environment could change either the chemical configuration of the defect site or the oscillator strength of the optical transition, it could open nonradiative decay channels capable of quenching the PL emission. Similar substrate-induced PL quenching effects have been observed for the case of band-edge E_{11} excitons.[34−37]

Based on these studies, we conclude that, in the case of Figure 3a, the glass substrate, due to its more polar and charged environment, likely causes quenching of the emission of all the aryl-H configurations so that only the emission of the most abundant $OrthoL_{90}$ configuration remains observable. In the case of Figure 3c, a 160 nm polystyrene layer provides a degree of isolation from the glass substrate, such that sharp emission peaks beyond the 1190 nm band, due to the $ParaL_{90}$, $OrthoL_{30}$ and $ParaL_{-30}$ aryl-H configurations, become observable. The spread of PL peaks over almost the entire 1000−1350 nm spectral range in Figure 3e suggests that encapsulation of functionalized SWCNTs in polystyrene provides sufficient environmental isolation to observe all the possible defect-state transitions, as in the case of PFO-BPy wrapping.

Analyses on Shape and Width of Spectral Peaks. Comparing the emission peaks displayed in Figures 1 and 3 further shows that the shape and width of the spectral lines change dramatically with dielectric environment. In the case of PFO-BPy-wrapped aryl-functionalized SWCNTs, almost all the PL peaks are characterized by line widths <5 meV (Figure 4a). Twenty of 50 PL peaks investigated already display resolution-limited line width values of about 2 meV in these measurements that have been carried out with a low-resolution (1/8 m) spectrometer to cover the entire emission range of the functionalized SWCNTs (950−1350 nm) in a single spectrum. Thus, to further investigate the limits of defect-related line widths for the well-isolated PFO-BPy-wrapped SWCNTs, we repeated measurements for the 20 narrowest emission peaks using a high-resolution spectrometer system capable of ~0.25 meV spectral resolution. These measurements revealed sharp defect emission peaks that can be fitted with a Lorentzian function and have Lorentzian line width as narrow as 0.278 meV with an average fwhm of ~0.4 meV, as shown in Figure 4b. A plot of the fwhm values as a function of emission wavelength (Figure S7a) shows no correlation between the two variables indicating that the exciton dephasing that dominates the contribution to the spectral line widths of the quantum defects is independent of the confinement energy in these cases.

A closer look at the line shape on a logarithmic scale reveals that almost all of the sharp lines from quantum defects in PFO-BPy-wrapped SWCNTs show strong sidebands that reside predominantly on the low energy side of the zero-phonon line (ZPL), as shown exemplarily for three cases in Figure 4c−e (open dots). These peculiar line shapes have previously been observed in low-T PL spectra of E_{11} band-edge excitons and can be simulated with a model that considers the interplay between localized excitons and localized acoustic phonons.[38−41] The solid lines in Figure 4c−e are simulated line shapes generated by applying this same model to the aryl-H defect-state emission. The exciton emission line shapes are calculated by taking the mirror image of the absorption spectrum, which itself is derived from the imaginary part of the Fourier transform of the linear susceptibility in response to a δ-shaped laser pulse. The model accounts for localization of both excitons and acoustic phonons, which we suggest is mediated by the copolymer backbone, as described in detail in our previous work on unfunctionalized PFO-BPy-wrapped SWCNTs.[40] Good agreement is found by varying the phonon confinement length in the range of 5−28 nm while keeping the exciton confinement length of 3.4−3.6 nm and the acoustic phonon barrier height of 1.3−1.5 meV nearly constant. The latter corresponds to the peak separation between the ZPL and the phonon wings. The exciton confinement length of 3.4−3.6 nm is also in good agreement with the ~2.7−3.9 nm orbital distribution of the transition densities for the four lowest energy aryl-H configurations yielded by quantum chemistry computation (Figure S5). This analysis demonstrates that this model not only is applicable to band-edge excitons (E_{11}) as in

DOI: 10.1021/acsnano.7b03022
ACS Nano 2017, 11, 10785−10796

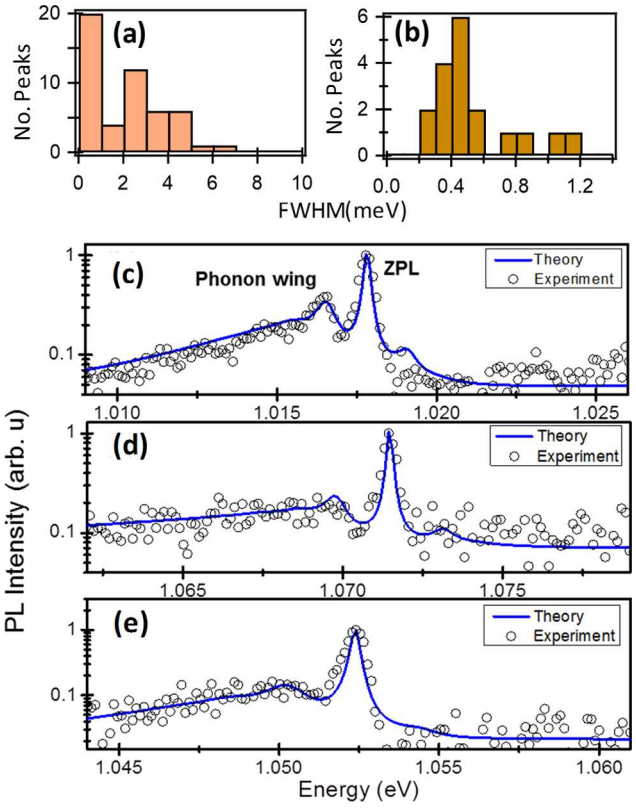

Figure 4. Histogram showing distribution of spectral line widths (fwhm) determined from Lorentzian fits of individual defect states of PFO-BPy-wrapped 3,5-dichlorobenzene-functionalized SWCNTs measured using low-resolution (a) and high-resolution (b) spectrometers. High-resolution spectra were taken only on the PL peaks with fwhm <2 meV. (c−e) High-resolution PL spectra of 3 individual defect states (circles) plotted on a log-scale. Blue solid lines: calculated PL spectra including exciton and phonon localization effects mediated by the PFO-BPy wrapping that gives rise to pronounced side-band-resolved acoustic phonon wings and ultranarrow zero phonon line (ZPL) width.

previous work[38−41] but also effectively describes the defect-bound excitons introduced by the functionalization procedures.

For comparison, a detailed analysis of the line widths of DOC-wrapped aryl-functionalized SWCNTs deposited directly on glass is shown in Figure 5a. While the spectral lines in the E_{11} emission range (<1020 nm) appear relatively narrow (fwhm <5 meV), as expected for cryogenic experiments, all spectral lines in the 1080−1190 nm range of the Ortho L_{90} transition are characterized with a fwhm >5 meV (average fwhm ∼10 meV). The line width *vs* emission wavelength plot (Figure S7b) again shows no correlation between these two parameters in the 1080−1190 nm range. These broad peaks stand in stark contrast to the narrow peaks observed for PFO-BPy-wrapped SWCNTs and suggest that the nonradiative and spectral diffusion processes introduced by the glass substrate partially quench and broaden the OrthoL_{90} transition.

It is interesting to note that the rather symmetric Lorentzian lines with significantly narrower fwhm's of 2−5 meV (Figure 3c and Figure S7b) appear in the 1166−1250 nm spectral range when DOC-wrapped and functionalized SWCNTs are deposited onto 160 nm polystyrene. The narrow line widths of these peaks, likely originating from OrthoL_{90} and ParaL_{90} transitions, suggest that the polystyrene layer provides some degree of isolation from undesired spectral diffusion effects

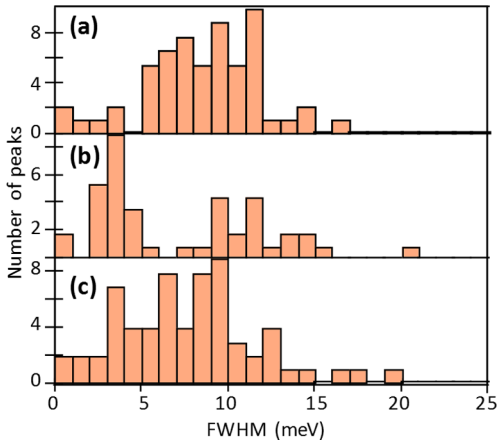

Figure 5. Histograms showing the line width (fwhm) distribution of the PL peaks of individual quantum defects of DOC-wrapped 4-methoxybenzene-functionalized SWCNTs deposited directly on glass (a), on 160 nm thick polystyrene layer (b), and sandwiched between two polystyrene layers (c). 50, 46, and 62 PL peaks observed on PL spectra of 40, 39, and 40 individual SWCNTs are analyzed for (a), (b) and (c), respectively.

found for the glass substrate,[31] albeit still inferior to the isolation provided by PFO-BPy wrapping that results in sub-meV line widths. Complete encapsulation into top and bottom polystyrene layers in Figure 3e on the other hand results in significant broadening of PL peaks. In contrast to the case of SWCNT on glass (Figure 3a and Figure 5a), the spectral peaks are highly asymmetric with broadening appearing mostly on the long wavelength side. Prior low-*T* PL studies of the E_{11} band-edge exciton revealed that such asymmetric PL peaks result from merging of the acoustic phonon sideband and ZPL, which are separated by an energy gap in the case of PFO-BPy-wrapped tubes. The Ohmic model, proposed by Galland *et al.*,[39] explains that this merging occurs because the localized exciton of the defect state dephases *via* interaction with unconfined, 1D acoustic phonons. The finding therefore suggests that the addition of the top polystyrene layer not only makes all the transitions of aryl-H quantum defects emissive but also may lead to enhancement of the exciton−acoustic phonon interaction and removal of acoustic phonon barriers that are responsible for the emergence of sharp symmetric spectral peaks.

Pump-Dependent Evolution of a Quantum Defect. Finally, we investigate the pump-dependent evolution of a quantum defect for a PFO-BPy-wrapped 3,5-dichlorobenzene-functionalized SWCNT to evaluate the suitability as a quantum light source with good spectral purity. The data in Figure 6a show several transitions in the vicinity of the E_{11} band-edge exciton, while the defect related emission around 1.07 eV appears as a solitary spectral line. Figure 6b shows that the emission intensities for both exciton species initially increase linearly at low pump power (<0.2 mW). At higher pump powers, the total intensity of the E_{11} emission saturates moderately while the defect-state emission strongly saturates and even quenches at the highest pump powers. The latter effect can be caused either by photoinduced damage[42] or by quantum coupling of the defect-state exciton to higher energy excitons, similar to the behavior of quantum dot excitons that quench reversibly in favor of biexciton emission at highest pump power.[43] Importantly, despite more than 3 orders of magnitude increase in pump power, neither additional PL peaks

DOI: 10.1021/acsnano.7b03022
ACS Nano 2017, 11, 10785−10796

from the high energy excited states nor background extending from the tail of the band-edge emission arises on the high-energy side of the PL peak of the quantum defect. As a result, the PL peak of the defect remains completely isolated, revealing that defect states in PFO-BPy-wrapped SWCNTs can maintain the emission characteristics of a 2 level system up to very high pump powers. In accordance with these findings, our recent second order photon correlation experiments on such quantum defects demonstrate room temperature single-photon emission with 99% purity (*i.e.*, $g^{(2)}(0) < 0.01$).[17]

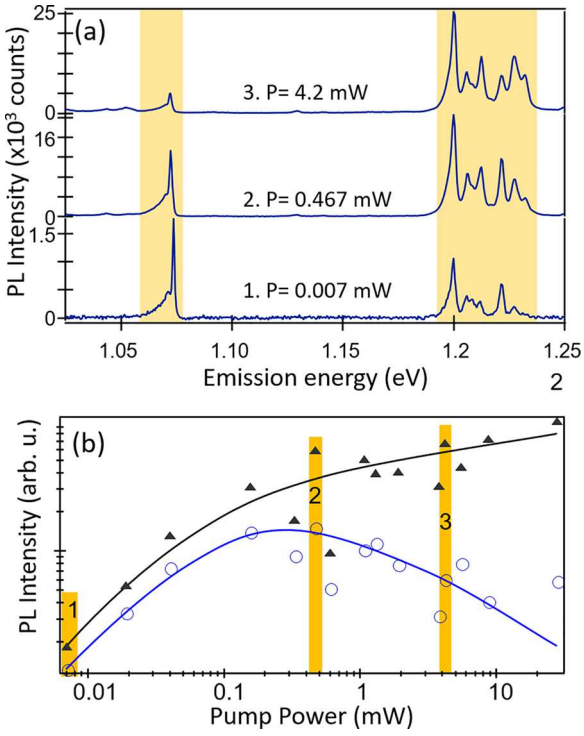

Figure 6. (a) Pump-power-dependent PL spectra of a PFO-BPy-wrapped 3,5-dichlorobenzene-functionalized SWCNT. (b) PL intensity of the defect emission (blue) and E_{11} band-edge exciton (black) integrated from the spectral bands highlighted in yellow. The yellow bars labeled 1−3 in (b) mark the pump powers where the spectra of (a) are acquired. The solid lines are given as guides for the eye. While PL of the band-edge emission intensity grows continuously with pump power, PL of the defect emission saturates and quenches at higher pump powers. Spectral line widths remain below 4 meV for all the pump powers.

CONCLUSIONS

Our previous study on oxygen-functionalized SWCNTs revealed that covalent attachment of ether and epoxide functional groups can occur in three different stable configurations: ether-l, ether-d and epoxide-l, each of which create distinct quantum defect states with optical emission at 1050, 1100, and 1280 nm, respectively (-l/-d represents the parallel/perpendicular alignments between C−O−C bonds and the tube axis).[7] Similarly, our present work suggests a more complex picture for monovalent aryl functionalization, which can yield six distinct aryl-H binding configurations. A qualitative correspondence between the computational results and the distribution of experimentally observed PL peaks indicates that these multiple binding configurations are the likely origin of our experimentally observed broad spectral diversity from the defect state PL. Furthermore, this diversity allows PL emission to span the telecom O-band (1260−1360 nm) and presents the possibility of extending even further to the 1.55 μm telecom C-band *via* the use of larger diameter SWCNTs.[17] These findings stand in contrast to the recent report that divalent aryl functional groups are necessary to create deep trap states emitting at wavelengths beyond 1190 nm for (6,5) SWCNTs.[13] The agreement we find between experimental results and quantum chemical modeling may thus serve as a starting point for understanding the diversity of reported solution PL spectra of sp^3-functionalized SWCNTs.[11−14] In particular, preferential generation of specific, chemically distinct, binding configurations may likely be determined by controlling the interplay of nanotube chirality with specific SWCNT surface structures, providing a possible basis for devising strategies to direct binding to preselected configurations. Furthermore, our study shows that emission intensity as well as the shape and widths of spectral peaks of specific aryl-H configurations can be manipulated *via* environmental interactions. Ultimately, our study provides evidence that aryl functionalization can give rise to defect states with deeper spectral red-shifts and better emission characteristics (*i.e.*, narrower line widths and better spectral isolation) compared to those of oxygen defect states.

METHODS

SWCNT Sample Preparation. Single-chirality (6,5) SWCNTs in 1% sodium deoxycholate (DOC) were prepared from CoMoCAT SG65i (Sigma-Aldrich) starting material by using a two-step aqueous two-phase extraction process.[44] PFO-BPy (poly[(9,9-dioctylfluorenyl-2,7-diyl)-*alt*-co-(6,6′)])-wrapped (6,5) SWCNTs were isolated in toluene suspensions by a separation method as described previously.[45,46] Two types of functionalization processes were used to dope chirality-enriched SWCNTs. The first is a solution doping method established previously.[22,26] DOC-wrapped (6,5) SWCNT samples are first exchanged into 1% (w/v) sodium dodecyl sulfate (SDS) by ultrafiltration. Fifty microliters of doping solution (0.1 mg/mL of 4-methoxybenzene diazonium salt in water) was then added to 1 mL of the SWCNT solution, adjusted to a concentration for which an optical density of ∼0.1 is obtained at the E_{11} absorption peak. The reaction is monitored *via* PL spectroscopy and the progress is stopped after attaining the desired defect-state PL level by exchanging the samples into 1% (w/v) DOC. Functionalized DOC-wrapped (6,5) SWCNTs were spin-coated onto glass coverslips with three different configurations: (a) directly spin-coating on glass coverslips, (b) spin-coating on glass coverslips coated by a 160 nm polystyrene layer, (c) SWCNTs are sandwiched between two layers of 160 nm polystyrene layer on glass coverslips. The second functionalization method is based on a dip-doping process and used on PFO-BPy-wrapped (6,5) nanotubes. The SWCNTs are first spin-coated on a glass cover coated by a thin layer of polystyrene (∼160 nm). The substrate is then immersed in an aqueous solution of 3,5-dichlorobenzene diazonium (0.7 mg/mL in nanopure water) or exposed to a droplet of the same solution for 3−5 min. The doping process is stopped by putting the substrate into 1% (w/v) DOC for another 3 min. The substrate containing functionalized SWCNTs is then completely dried in air and ready for optical measurements. We note that this process was found to be not effective when 4-methoxybenzene diazonium was used as the dopant.

Low-Temperature Optical Measurements. Spectroscopic measurements were performed on a home-built microscope-PL system at temperatures between 3.9 and 5 K. Functionalized SWCNT samples were loaded into a continuous-flow liquid He cryostat (Oxford Instruments). A continuous-wave (CW) Ti:sapphire laser at 854 nm was used to excite (6,5) SWCNTs at the E_{11} phonon sideband with an average power of ∼2 μW. An infrared objective (Olympus) with NA = 0.65 and 50× magnification was used for laser illumination and collection of the PL signal. The laser beam is focused into the objective

DOI: 10.1021/acsnano.7b03022
ACS Nano 2017, 11, 10785−10796

to achieve ~40 μm diameter illumination area for the wide-field imaging mode. We used this mode to inspect whether the samples have the desired single tube density of not more than ~1 nanotube/4 μm^2 as well as to discriminate between single tubes and tube bundles (the images of tube bundles are a few times larger in spatial extent than those of the individual ones). The PL spectra of selected single tubes were then excited and collected in confocal mode, in which the laser is focused to a diffraction-limited spot. The PL images and spectra were acquired with a two-dimensional InGaAs array camera and one-dimensional InGaAs linear array detector, respectively.

Computational Methodology. The model systems for this study (Figure 2a) were constructed with finite-length SWCNT segments of three unit cells (~12 nm) in length, terminated with hydrogen atoms at all edge positions to passivate dangling bonds. This size is much larger than the size of excitons (*i.e.*, separation between an electron and a hole) in the (6,5) SWCNT.[47] Subsequently, considered tubes are long enough to eliminate the majority of artificial edge effects originating from a finite size of the nanotube. All quantum-chemical calculations were performed with the commercially available Gaussian09 software package.[48] Optimizations of the ground- and excited-state geometries were performed using DFT with the long-range corrected CAM-B3LYP functional[49] and STO-3G basis set.[50,51] This methodology has been previously extensively applied to both pristine[52,53] and functionalized[7,54] SWCNTs, demonstrating good qualitative agreement with experimental data. For the $OrthoL_{30}$ case, geometry optimization was performed in the dielectric environment of solvents introduced by the conductor polarized continuum model.[55,56] We observe that variation of the dielectric environment from heptane (ε = 1.9113) to water (ε = 78.3553) shows very little differences in the total energy or the structural characteristics. As such, all results presented here were computed using geometries optimized in vacuum. The reaction mechanism behind covalent functionalization with aryl diazonium reagents requires that a pair of chemical species tie up two electrons from the π-electron system of the carbon nanotube, attaching in close proximity at the same carbon ring to result in emission.[20,21] In our aryl-H model, this pair includes 4-bromobenzene and hydrogen, resulting in 6 topologically unique binding configurations at the (6,5) SWCNT sidewall: three distinct Para and three Ortho configurations, which are identified according to the direction of aryl-H arrangement relative to the SWCNT lattice and labeled as L_{30}, L_{90}, and L_{-30}, where the subscript describes the approximate angle between a vector lying along the bond and the SWCNT axis, as illustrated in Figure 2a. For (6,5) SWCNTs, these angles are more precisely 27, 87, and −33° for L_{30}, L_{90}, and L_{-30}, respectively.

To test the expectation that the aryl-H structure is a reasonable model for describing defects associated with the more complex aryl derivatives used in the experiments, we also performed DFT calculations for an unsubstituted aryl group as a dopant. We note that the combined study of pristine aryl and 4-bromobenzene spans the electronegativity range of the 4-methoxybenzene and 3,5-dichlorobenzene used experimentally. In line with expectations, our calculations for (6,5) SWCNT functionalized by pristine aryl and hydrogen (Figure S2, Supporting Information) yield an energy level diagram essentially identical to that of 4-bromobenzene for all 6 binding configurations. We also recognize the potential for hydroxide to bind to the nanotube surface as an alternative to the proton in our aqueous environment. Substituting OH for H attached to the same carbon-ring of the nanotube as the 4-bromobenzene (resulting in aryl−OH configurations) provides negligible changes in the electronic structure of the functionalized (6,5) SWCNT (Figure S3, Supporting Information). Such insensitivity to the chemical composition of a functional group agrees with our previous computational study[54] of tip-functionalized (10,5) SWCNT, where we have found that variations in electron withdrawing/donating properties of the capping groups at the edges of finite size SWCNTs play a very minor role in changing the HOMO−LUMO gaps and optical spectra of systems. Overall these findings validate applicability of our aryl-H model for computational studies of defect states in covalently functionalized SWCNTs.

Time-dependent density functional theory calculations were performed with the same functional and basis set as was applied for ground-state geometry optimizations. Fifteen excited states were calculated to represent the absorption spectra in the range of 1000−1400 nm. The energy of the emission state and its oscillator strength were calculated by using TD-DFT optimal geometry of the lowest energy excited state. Natural transition orbitals[57] were used to characterize the degree of delocalization of exciton wave function along the SWCNT in the region of the defect. The direct comparison of the calculated optical spectra with the respective experimental data is not practical because of the mismatch in the transition energies originating from three distinct reasons: (i) incomplete basis set of a relatively small size (here STO-3G), (ii) self-interaction error in the density functional (here CAM-B3LYP model), and (iii) confinement effect introduced by the finite size of the SWCNT segments (here 12 nm). All three factors lead to significant blue-shifts of transition energies compared to experiment, as has been already discussed in the literature.[52,53] For our systems, the first two errors belong to the "methodology error" and are expected to identically affect all aryl-H configurations, independent of the position of the sp^3-defect introduced by aryl functionalization of the SWCNT. In contrast, the third factor (called the confinement error) is expected to be sensitive to the degree of spatial delocalization of an exciton along the nanotube. Because localization of the lowest energy bright exciton around the defect site increases for aryl-H configurations exhibiting the most red-shifted optical transitions (Figure S5 in Supporting Information), the confinement error varies across the binding configurations. Those excitons that are more strongly localized (*e.g.*, $ParaL_{-30}$ and $OrthoL_{30}$ configurations) have the smallest confinement error, whereas excitons that exhibit delocalization across the entire nanotube (*e.g.*, $ParaL_{30}$ and $OrthoL_{-30}$ configurations) are the most affected by the confinement. This trend is clearly seen in Figure S9a depicting the correlation between the tube's length (varying from 1 (~4 nm) to 4 (~16 nm) lattice units in length) and the energy of the lowest bright transition in aryl-H Para conformations.

As such, in order to match experimental data, an appropriate correction factor to the calculated transition energies should include two independent components: one is a constant shift across all systems accounting for the methodology error and one system-dependent component accessing the confinement error. The methodology error can be defined as a difference between the experimental energy of the main E_{11} band of the pristine SWCNT and the extrapolated E_{11} energy of an infinitely long nanotube model, resulting in the constant and uniform red-shift of 0.6675 eV (technical details are presented in Table S1, Figure S9b, and discussed in Supporting Information). The confinement error introduced by the finite size of the SWCNT models depends on the exciton localization about the defect site and has to be introduced to varying degrees dependent on the red-shifts of defect-state emission energy (designated as E_{11}^*) in the aryl-H system with respect to the E_{11} emission of the pristine nanotube, according to observables depicted in Figure S5. To find this scaling factor, we correlate the energy of the lowest energy exciton, $E_{11}^*(\infty)$, of aryl-functionalized infinite SWCNT, estimated as *Y*-intercepts from Figure S9a, with the energy difference between the E_{11} emission of the pristine SWCNT and the E_{11}^* emission of aryl-H conformations using our finite 3-unit cell nanotube model. This dependence shown in Figure S9b demonstrates a nearly linear behavior with a slope (~0.5945) corresponding to the scaling factor defining the confinement error. As such, the scaled emission energies corrected for both the methodology error and the confinement error satisfy the following equation:

$$E_{11,\mathrm{scaled}}^{*} = 0.5945(E_{11}^{*} - E_{11}) + E_{11}^{\mathrm{exp}} \quad (1)$$

Substituting the calculated emission energies of the functionalized and pristine SWCNTs of 3 lattice units in length used in our calculations (Table S1) and the experimental value of E_{11}^{exp} = 1.2498 eV of the main E_{11} emissive peak to eq 1, one can get the scaled emission energies that can be directly compared with experimental data.

DOI: 10.1021/acsnano.7b03022
ACS Nano 2017, 11, 10785−10796

ASSOCIATED CONTENT

Supporting Information

The Supporting Information is available free of charge on the ACS Publications website at DOI: 10.1021/acsnano.7b03022.

Calculated relative total energies of each aryl-H binding configuration comparing energetic stabilities of different configurations; comparison of the ground-state electronic structure of (6,5) SWCNTs functionalized with 4-bromozbenzene *vs* pristine aryl and hydrogen *vs* hydroxide binding; simulated absorption spectrum with the absorption oscillator strengths and the lowest energy emission oscillator strength for a 6,5 SWCNT functionalized with 4-bromobenzene and hydrogen in paraL_{-30} configuration; calculated localization of the holes and electrons for the lowest energy emission state for different binding configurations of 4-bromobenzene/hydrogen-functionalized (6,5) SWCNT; absorption spectra calculated in vacuum and in the dielectric environment of heptane, acetonitrile, and water for pristine (6,5) SWCNTs and its functionalized counterpart with aryl-H configurations; plot of fwhm of the PL peak as a function of their emission wavelengths; low-temperature PL spectra of nine individual DOC-wrapped 3,5-dichlorobenzene-functionalized (6,5) SWCNTs deposited between two polystyrene layers; table of the lowest energy emission state and the first bright transition; plots to estimate the scaling parameter for transition energy evaluating the confinement and methodology errors in our calculations (PDF)

AUTHOR INFORMATION

Corresponding Authors

*E-mail: skdoorn@lanl.gov.
*E-mail: htoon@lanl.gov.

ORCID

Xiaowei He: 0000-0002-4982-8250
Nicolai F. Hartmann: 0000-0002-4174-532X
Svetlana V. Kilina: 0000-0003-1350-2790
Stefan Strauf: 0000-0002-9887-7059
Jeffrey L. Blackburn: 0000-0002-9237-5891
Sergei Tretiak: 0000-0001-5547-3647
Stephen K. Doorn: 0000-0002-9535-2062
Han Htoon: 0000-0003-3696-2896

Notes

The authors declare no competing financial interest.

ACKNOWLEDGMENTS

This work was conducted, in part, at the Center for Nonlinear Studies and the Center for Integrated Nanotechnologies, a U.S. Department of Energy, Office of Basic Energy Sciences user facility and supported in part by Los Alamos National Laboratory (LANL) Directed Research and Development Funds. S.S. acknowledges financial support by the National Science Foundation (NSF) under awards DMR-1506711 and ECCS-MRI-1531237. NREL researchers were supported by the Solar Photochemistry Program of the U.S. Department of Energy, Office of Science, Basic Energy Sciences, Division of Chemical Sciences, Geosciences and Biosciences, under Contract No. DE-AC36-08GO28308 to NREL. S.K. acknowledges NSF Grant CHE-1413614 for financial support of studies of functionalized carbon nanotubes and the Alfred P. Sloan Research Fellowship BR2014-073 for partial support of studies of surface effects at interfaces of nanostructures. For computational resources and administrative support, we thank the Center for Computationally Assisted Science and Technology (CCAST) at North Dakota State University and the National Energy Research Scientific Computing Center (NERSC) allocation awards 86678, supported by the Office of Science of the DOE under contract No. DE-AC02-05CH11231. We also acknowledge the LANL Institutional Computing (IC) Program for providing computational resources.

REFERENCES

(1) Koenraad, P. M.; Flatte, M. E. Single Dopants in Semiconductors. *Nat. Mater.* **2011**, *10*, 91−100.
(2) Wolf, S.; Awschalom, D.; Buhrman, R.; Daughton, J.; Von Molnar, S.; Roukes, M.; Chtchelkanova, A. Y.; Treger, D. Spintronics: A Spin-based Electronics Vision for the Future. *Science* **2001**, *294*, 1488−1495.
(3) Bol, A. A.; van Beek, R.; Meijerink, A. On the Incorporation of Trivalent Rare Earth Ions in II−VI Semiconductor Nanocrystals. *Chem. Mater.* **2002**, *14*, 1121−1126.
(4) Schirhagl, R.; Chang, K.; Loretz, M.; Degen, C. L. Nitrogen-acancy Centers in Diamond: Nanoscale Sensors for Physics and Biology. *Annu. Rev. Phys. Chem.* **2014**, *65*, 83−105.
(5) Aharonovich, I.; Greentree, A. D.; Prawer, S. Diamond Photonics. *Nat. Photonics* **2011**, *5*, 397−405.
(6) Aharonovich, I.; Castelletto, S.; Simpson, D. A.; Su, C. H.; Greentree, A. D.; Prawer, S. Diamond-based Single-Photon Emitters. *Rep. Prog. Phys.* **2011**, *74*, 076501.
(7) Ma, X.; Adamska, L.; Yamaguchi, H.; Yalcin, S. E.; Tretiak, S.; Doorn, S. K.; Htoon, H. Electronic Structure and Chemical Nature of Oxygen Dopant States in Carbon Nanotubes. *ACS Nano* **2014**, *8*, 10782−10789.
(8) Miyauchi, Y.; Iwamura, M.; Mouri, S.; Kawazoe, T.; Ohtsu, M.; Matsuda, K. Brightening of Excitons in Carbon Nanotubes on Dimensionality Modification. *Nat. Photonics* **2013**, *7*, 715−719.
(9) Ghosh, S.; Bachilo, S. M.; Simonette, R. A.; Beckingham, K. M.; Weisman, R. B. Oxygen Doping Modifies Near-infrared Band Gaps in Fluorescent Single-Walled Carbon Nanotubes. *Science* **2010**, *330*, 1656−1659.
(10) Ma, X.; Baldwin, J. K.; Hartmann, N. F.; Doorn, S. K.; Htoon, H. Solid-State Approach for Fabrication of Photostable, Oxygen-Doped Carbon Nanotubes. *Adv. Funct. Mater.* **2015**, *25*, 6157−6164.
(11) Piao, Y. M.; Meany, B.; Powell, L. R.; Valley, N.; Kwon, H.; Schatz, G. C.; Wang, Y. H. Brightening of Carbon Nanotube Photoluminescence Through the Incorporation of sp^3 Defects. *Nat. Chem.* **2013**, *5*, 840−845.
(12) Maeda, Y.; Minami, S.; Takehana, Y.; Dang, J.-S.; Aota, S.; Matsuda, K.; Miyauchi, Y.; Yamada, M.; Suzuki, M.; Zhao, R.-S.; Zhao, X.; Nagase, S. Tuning of the Photoluminescence and Up-Conversion Photoluminescence Properties of Single-Walled Carbon Nanotubes by Chemical Functionalization. *Nanoscale* **2016**, *8*, 16916−16921.
(13) Shiraki, T.; Shiraishi, T.; Juhász, G.; Nakashima, N. Emergence of New Red-Shifted Carbon Nanotube Photoluminescence Based on Proximal Doped-Site Design. *Sci. Rep.* **2016**, *6*, 28393.
(14) Kwon, H.; Furmanchuk, A. o.; Kim, M.; Meany, B.; Guo, Y.; Schatz, G. C.; Wang, Y. Molecularly Tunable Fluorescent Quantum Defects. *J. Am. Chem. Soc.* **2016**, *138*, 6878−6885.
(15) Kwon, H.; Kim, M.; Meany, B.; Piao, Y.; Powell, L. R.; Wang, Y. Optical Probing of Local pH and Temperature in Complex Fluids with Covalently Functionalized, Semiconducting Carbon Nanotubes. *J. Phys. Chem. C* **2015**, *119*, 3733−3739.
(16) Ma, X.; Hartmann, N. F.; Baldwin, J. K. S.; Doorn, S. K.; Htoon, H. Room Temperature Single-Photon Generation from Solitary Dopants of Carbon Nanotubes. *Nat. Nanotechnol.* **2015**, *10*, 671.
(17) He, X.; Hartmann, N. F.; Ma, X.; Kim, Y.; Ihly, R.; Blackburn, J. L.; Gao, W.; Kono, J.; Yomogida, Y.; Hirano, A.; Tanaka, T.; Kataura, H.; Htoon, H.; Doorn, S. K. Tunable Room-Temperature Single-

DOI: 10.1021/acsnano.7b03022
ACS Nano 2017, 11, 10785−10796

Photon Emission at Telecom Wavelengths from sp^3 Defects in Carbon Nanotubes. *Nat. Photonics* **2017**, *11*, 577−582.
(18) Khasminskaya, S.; Pyatkov, F.; Słowik, K.; Ferrari, S.; Kahl, O.; Kovalyuk, V.; Rath, P.; Vetter, A.; Hennrich, F.; Kappes, M. M.; Gol'tsman, G.; Korneev, A.; Rockstuhl, C.; Krupke, R.; Pernice, W. H. Fully Integrated Quantum Photonic Circuit with an Electrically Driven Light Source. *Nat. Photonics* **2016**, *10*, 727−732.
(19) Pyatkov, F.; Fütterling, V.; Khasminskaya, S.; Flavel, B. S.; Hennrich, F.; Kappes, M. M.; Krupke, R.; Pernice, W. H. Cavity-Enhanced Light Emission From Electrically Driven Carbon Nanotubes. *Nat. Photonics* **2016**, *10*, 420−427.
(20) Kilina, S.; Ramirez, J.; Tretiak, S. Brightening of the Lowest Exciton in Carbon Nanotubes *via* Chemical Functionalization. *Nano Lett.* **2012**, *12*, 2306−2312.
(21) Ramirez, J.; Mayo, M. L.; Kilina, S.; Tretiak, S. Electronic Structure and Optical Spectra of Semiconducting Carbon Nanotubes Functionalized by Diazonium Salts. *Chem. Phys.* **2013**, *413*, 89−101.
(22) Hartmann, N. F.; Velizhanin, K. A.; Haroz, E. H.; Kim, M.; Ma, X.; Wang, Y.; Htoon, H.; Doorn, S. K. Photoluminescence Dynamics of Aryl sp3 Defect States in Single-Walled Carbon Nanotubes. *ACS Nano* **2016**, *10*, 8355−8365.
(23) Gordon, L.; Weber, J. R.; Varley, J. B.; Janotti, A.; Awschalom, D. D.; Van de Walle, C. G. Quantum Computing with Defects. *MRS Bull.* **2013**, *38*, 802−807.
(24) Loncar, M.; Faraon, A. Quantum Photonic Networks in Diamond. *MRS Bull.* **2013**, *38*, 144−148.
(25) Iwamura, M.; Akizuki, N.; Miyauchi, Y.; Mouri, S.; Shaver, J.; Gao, Z.; Cognet, L.; Lounis, B.; Matsuda, K. Nonlinear Photoluminescence Spectroscopy of Carbon Nanotubes with Localized Exciton States. *ACS Nano* **2014**, *8*, 11254−11260.
(26) Hartmann, N. F.; Yalcin, S. E.; Adamska, L.; Hároz, E. H.; Ma, X.; Tretiak, S.; Htoon, H.; Doorn, S. K. Photoluminescence Imaging of Solitary Dopant Sites in Covalently Doped Single-wall Carbon Nanotubes. *Nanoscale* **2015**, *7*, 20521−20530.
(27) Usrey, M. L.; Lippmann, E. S.; Strano, M. S. Evidence for a Two-Step Mechanism in Electronically Selective Single-Walled Carbon Nanotube Reactions. *J. Am. Chem. Soc.* **2005**, *127*, 16129−16135.
(28) Schmidt, G.; Gallon, S.; Esnouf, S.; Bourgoin, J. P.; Chenevier, P. Mechanism of the Coupling of Diazonium to Single-Walled Carbon Nanotubes and Its Consequences. *Chem. - Eur. J.* **2009**, *15*, 2101−2110.
(29) Hilmer, A. J.; McNicholas, T. P.; Lin, S.; Zhang, J.; Wang, Q. H.; Mendenhall, J. D.; Song, C.; Heller, D. A.; Barone, P. W.; Blankschtein, D.; Strano, M. S. Role of Adsorbed Surfactant in the Reaction of Aryl Diazonium Salts with Single-Walled Carbon Nanotubes. *Langmuir* **2012**, *28*, 1309−1321.
(30) Kilina, S.; Kilin, D.; Tretiak, S. Light-Driven and Phonon-Assisted Dynamics in Organic and Semiconductor Nanostructures. *Chem. Rev.* **2015**, *115*, 5929−5978.
(31) Okuno, K.; Shigeta, Y.; Kishi, R.; Miyasaka, H.; Nakano, M. Tuned CAM-B3LYP Functional in the Time-Dependent Density Functional Theory Scheme for Excitation Energies and Properties of Diarylethene Derivatives. *J. Photochem. Photobiol., A* **2012**, *235*, 29−34.
(32) Kobayashi, R.; Amos, R. D. The Application of CAM-B3LYP to the Charge-Transfer Band Problem of the Zincbacteriochlorin−Bacteriochlorin Complex. *Chem. Phys. Lett.* **2006**, *420*, 106−109.
(33) Tomasi, J.; Mennucci, B.; Cammi, R. Quantum Mechanical Continuum Solvation Models. *Chem. Rev.* **2005**, *105*, 2999−3094.
(34) Crochet, J. J.; Duque, J. G.; Werner, J. H.; Doorn, S. K. Photoluminescence Imaging of Electronic-Impurity-Induced Exciton Quenching in Single-Walled Carbon Nanotubes. *Nat. Nanotechnol.* **2012**, *7*, 126−132.
(35) Finnie, P.; Lefebvre, J. Photoinduced Band Gap Shift and Deep Levels in Luminescent Carbon Nanotubes. *ACS Nano* **2012**, *6*, 1702−1714.
(36) Hertel, T.; Himmelein, S.; Ackermann, T.; Stich, D.; Crochet, J. Diffusion Limited Photoluminescence Quantum Yields in 1-D Semiconductors: Single-Wall Carbon Nanotubes. *ACS Nano* **2010**, *4*, 7161−7168.
(37) Lee, A. J.; Wang, X.; Carlson, L. J.; Smyder, J. A.; Loesch, B.; Tu, X.; Zheng, M.; Krauss, T. D. Bright Fluorescence From Individual Single-Walled Carbon Nanotubes. *Nano Lett.* **2011**, *11*, 1636−1640.
(38) Ardizzone, V.; Chassagneux, Y.; Vialla, F.; Delport, G.; Delcamp, C.; Belabas, N.; Deleporte, E.; Roussignol, P.; Robert-Philip, I.; Voisin, C.; Lauret, J. S. Strong Reduction of Exciton-Phonon Coupling in Single-Wall Carbon Nanotubes of High Crystalline Quality: Insight into Broadening Mechanisms and Exciton Localization. *Phys. Rev. B: Condens. Matter Mater. Phys.* **2015**, *91*, 121410.
(39) Galland, C.; Högele, A.; Türeci, H. E.; Imamoğlu, A. Non-Markovian Decoherence of Localized Nanotube Excitons by Acoustic Phonons. *Phys. Rev. Lett.* **2008**, *101*, 067402.
(40) Sarpkaya, I.; Ahmadi, E. D.; Shepard, G. D.; Mistry, K. S.; Blackburn, J. L.; Strauf, S. Strong Acoustic Phonon Localization in Copolymer-Wrapped Carbon Nanotubes. *ACS Nano* **2015**, *9*, 6383−6393.
(41) Vialla, F.; Chassagneux, Y.; Ferreira, R.; Roquelet, C.; Diederichs, C.; Cassabois, G.; Roussignol, P.; Lauret, J.-S.; Voisin, C. Unifying the Low-Temperature Photoluminescence Spectra of Carbon Nanotubes: The Role of Acoustic Phonon Confinement. *Phys. Rev. Lett.* **2014**, *113*, 057402.
(42) Georgi, C.; Hartmann, N.; Gokus, T.; Green, A. A.; Hersam, M. C.; Hartschuh, A. Photoinduced Luminescence Blinking and Bleaching in Individual Single-Walled Carbon Nanotubes. *ChemPhysChem* **2008**, *9*, 1460−1464.
(43) Gerardot, B. D.; Strauf, S.; de Dood, M. J. A.; Bychkov, A. M.; Badolato, A.; Hennessy, K.; Hu, E. L.; Bouwmeester, D.; Petroff, P. M. Photon Statistics from Coupled Quantum Dots. *Phys. Rev. Lett.* **2005**, *95*, 137403.
(44) Hartmann, N. F.; Pramanik, R.; Dowgiallo, A.-M.; Ihly, R.; Blackburn, J. L.; Doorn, S. K. Photoluminescence Imaging of Polyfluorene Surface Structures on Semiconducting Carbon Nanotubes: Implications for Thin Film Exciton Transport. *ACS Nano* **2016**, *10*, 11449−11458.
(45) Subbaiyan, N. K.; Cambré, S.; Parra-Vasquez, A. N. G.; Hároz, E. H.; Doorn, S. K.; Duque, J. G. Role of Surfactants and Salt in Aqueous Two-Phase Separation of Carbon Nanotubes toward Simple Chirality Isolation. *ACS Nano* **2014**, *8*, 1619−1628.
(46) Fagan, J. A.; Khripin, C. Y.; Silvera Batista, C. A.; Simpson, J. R.; Hároz, E. H.; Hight Walker, A. R.; Zheng, M. Isolation of Specific Small-Diameter Single-Wall Carbon Nanotube Species via Aqueous Two-Phase Extraction. *Adv. Mater.* **2014**, *26*, 2800−2804.
(47) Lüer, L.; Hoseinkhani, S.; Polli, D.; Crochet, J.; Hertel, T.; Lanzani, G. Size and Mobility of Excitons in (6, 5) Carbon Nanotubes. *Nat. Phys.* **2009**, *5*, 54−58.
(48) Frisch, M. J.; Trucks, G. W.; Schlegel, H. B.; Scuseria, G. E.; Robb, M. A.; Cheeseman, J. R.; Scalmani, G.; Barone, V.; Mennucci, B.; Petersson, G. A.; et al. *Gaussian 09*; Gaussian, Inc.: Wallingford, CT, 2009.
(49) Yanai, T.; Tew, D. P.; Handy, N. C. A New Hybrid Exchange−Correlation Functional Using the Coulomb-Attenuating Method (CAM-B3LYP). *Chem. Phys. Lett.* **2004**, *393*, 51−57.
(50) Hehre, W. J.; Stewart, R. F.; Pople, J. A. Self-Consistent Molecular-Orbital Methods. I. Use of Gaussian Expansions of Slater-Type Atomic Orbitals. *J. Chem. Phys.* **1969**, *51*, 2657−2664.
(51) Collins, J. B.; Schleyer, P. v. R.; Binkley, J. S.; Pople, J. A. Self-Consistent Molecular Orbital Methods. XVII. Geometries and Binding Energies of Second-Row Molecules. A Comparison of Three Basis Sets. *J. Chem. Phys.* **1976**, *64*, 5142−5151.
(52) Kilina, S.; Tretiak, S. Excitonic and Vibrational Properties of Single-Walled Semiconducting Carbon Nanotubes. *Adv. Funct. Mater.* **2007**, *17*, 3405−3420.
(53) Kilina, S.; Badaeva, E.; Piryatinski, A.; Tretiak, S.; Saxena, A.; Bishop, A. R. Bright and Dark Excitons in Semiconductor Carbon Nanotubes: Insights from Electronic Structure Calculations. *Phys. Chem. Chem. Phys.* **2009**, *11*, 4113−23.

DOI: 10.1021/acsnano.7b03022
ACS Nano 2017, 11, 10785−10796

(54) Sharma, A.; Gifford, B. J.; Kilina, S. Tip Functionalization of Finite Single-Walled Carbon Nanotubes and Its Impact on the Ground and Excited State Electronic Structure. *J. Phys. Chem. C* **2017**, *121*, 8601−8612.
(55) Cossi, M.; Rega, N.; Scalmani, G.; Barone, V. Energies, Structures, and Electronic Properties of Molecules in Solution with the C-PCM Solvation Model. *J. Comput. Chem.* **2003**, *24*, 669−681.
(56) Barone, V.; Cossi, M.; Tomasi, J. Geometry Optimization of Molecular Structures in Solution by the Polarizable Continuum Model. *J. Comput. Chem.* **1998**, *19*, 404−417.
(57) Martin, R. L. Natural Transition Orbitals. *J. Chem. Phys.* **2003**, *118*, 4775−4777.

DOI: 10.1021/acsnano.7b03022
ACS Nano 2017, 11, 10785−10796